



## ISTITUTO NAZIONALE DI RICERCA METROLOGICA Repository Istituzionale

Comprehensive assessment of bioactive glass and glass-ceramic scaffold permeability: experimental measurements by pressure wave drop, modelling and computed tomography-

This is the author's accepted version of the contribution published as:

*Original*

Comprehensive assessment of bioactive glass and glass-ceramic scaffold permeability: experimental measurements by pressure wave drop, modelling and computed tomography-based analysis / Fiume, Elisa; Schiavi, Alessandro; Orlygsson, Gissur; Bignardi, Cristina; Verné, Enrica; Baino, Francesco. - In: ACTA BIOMATERIALIA. - ISSN 1742-7061. - 119:(2021), pp. 405-418. [10.1016/j.actbio.2020.10.027]

*Availability:*

This version is available at: 11696/71016 since: 2023-05-30T14:58:57Z

*Publisher:*

Elsevier

*Published*

DOI:10.1016/j.actbio.2020.10.027

*Terms of use:*

This article is made available under terms and conditions as specified in the corresponding bibliographic description in the repository

*Publisher copyright*

(Article begins on next page)

**Comprehensive assessment of bioactive glass and glass-ceramic scaffold permeability: experimental measurement by a pressure wave drop, modelling and computed tomography-based analysis**

Elisa Fiume<sup>a,b,1</sup>, Alessandro Schiavi<sup>c,1</sup>, Gissur Orlygsson<sup>d</sup>, Cristina Bignardi<sup>b</sup>, Enrica Verné<sup>a</sup>, Francesco Baino<sup>a,\*</sup>

<sup>a</sup> *Department of Applied Science and Technology (DISAT), Politecnico di Torino, 10129 Turin, Italy*

<sup>b</sup> *Department of Mechanical and Aerospace Engineering (DIMEAS), Politecnico di Torino, 10129 Turin, Italy*

<sup>c</sup> *National Institute of Metrological Research (INRiM), Applied Metrology and Engineering Division, 10135 Turin, Italy*

<sup>d</sup> *Department of Materials, Biotechnology and Energy, Innovation Center Iceland (ICI), 112 Reykjavik, Iceland*

\* Corresponding author: F. Baino

E-mail: francesco.baino@polito.it

<sup>1</sup> Both these authors contributed equally to the work.

## Abstract

Proper microstructural and transport properties are fundamental requirements for a suitable scaffold design and realization in tissue engineering applications. Scaffold microstructure (i.e. pore size, shape and distribution) and transport properties (i.e. intrinsic permeability), are commonly recognized as the key parameters related to the biological performance, such as cell attachment, penetration depth and tissue vascularization. While pore characteristics are relatively easy to assess, accurate and reliable evaluation of permeability still remains a challenge.

In the present study, the microstructural properties of foam-replicated bioactive glass-derived scaffolds (basic composition  $47.5\text{SiO}_2\text{--}2.5\text{P}_2\text{O}_5\text{--}20\text{CaO--}10\text{MgO--}10\text{Na}_2\text{O--}10\text{K}_2\text{O}$  mol.%) were determined as function of the sintering temperature within the range 600-850 °C, identified on the basis of thermal analyses that were previously performed on the material.

Scaffolds with total porosity between 55 and 84 vol.% and trabecular-like architecture were obtained, with pore morphological features varying according to the sintering temperature. Mathematical modelling, supported by micro-computed tomography ( $\mu$ -CT) imaging, was implemented to selectively investigate the effect of different pore features on intrinsic permeability, which was determined by laminar airflow alternating pressure wave drop measurements and found to be within  $0.051\text{--}2.811 \cdot 10^{-10}$  m<sup>2</sup>. The calculated effective porosity of the scaffolds was in the range of 46 to 66 vol.%, while the average pore diameter assessed by  $\mu$ -CT varied between 220 and 780  $\mu\text{m}$ , where the values in the lower range were observed for higher sintering temperatures (750-850 °C). Experimental results were critically discussed by means of a robust statistical analysis. Finally, the complete microstructural characterization of the scaffolds was achieved by applying the general constitutive equation based on Forchheimer's theory.

**Keywords:** Bioactive glass; Scaffold; Permeability; Porosity; Bone tissue engineering

## Nomenclature

$A_k$	Piston surface area	/m <sup>2</sup>
$A_p$	Pore surface area	/mm <sup>2</sup>
$A_s$	Scaffold cross sectional area	/mm <sup>2</sup>
$d_p$	Pore diameter	/mm
$d_t$	Throat diameter	/mm
$D_s$	Scaffold diameter	/mm
$f$	Piston oscillation frequency	/Hz
$f_c$	Friction factor	/dimensionless
$h$	Piston stroke (peak to peak)	/m
$k$	Intrinsic permeability	/m <sup>2</sup>
$L_s$	Scaffold length	/mm
$L_p$	Pore length	/mm
$m_s$	Scaffold mass	/g
$p_{rms}$	rms pressure	/Pa
$Q_v$	Volumetric flow rate	/m <sup>3</sup> · s <sup>-1</sup>
$q_{v,rms}$	rms volumetric airflow	/m <sup>3</sup> · s <sup>-1</sup>
$R$	Open-to-close pore volume ratio	/dimensionless
$R_i$	Interstitial Reynolds number	/dimensionless
$RH$	Relative humidity	/dimensionless
$T_{air}$	Air temperature	/°C
$T_s$	Sintering temperature	/°C
$T_x$	Crystallization onset	/°C
$T_c$	Maximum crystallization rate	/°C
$T_g$	Glass transition	/°C
$T_f$	Crystallization end	/°C
$U$	Linear flow velocity	/m · s <sup>-1</sup>
$V_p$	Pore volume	/mm <sup>3</sup>
$\beta$	Pore diameter/throat ratio	/dimensionless
$\partial P$	Pressure gradient	/Pa
$\Delta P$	Pressure differential	/Pa
$\varepsilon$	Scaffold effective porosity	/dimensionless
$\varepsilon_0$	Scaffold total porosity	/dimensionless
$\varepsilon_c$	Scaffold closed porosity	/dimensionless
$\phi_p$	Pore sphericity	/dimensionless
$\lambda$	Mean free path of air	/μm
$\mu$	Fluid dynamic viscosity	/Pa · s
$\rho$	Fluid density	/kg · m <sup>-3</sup>
$\rho_{app}$	Scaffold apparent density	/g · cm <sup>-3</sup>
$\rho_{glass}$	Glass density	/g · cm <sup>-3</sup>

## 1. Introduction

The need for bone repair has increased over the last decades due to the increase of elderly people worldwide [1]. When osseous tissue is irreversibly damaged owing to traumatic fractures, surgical removal of bone cancer or other pathologies, implantation of a bioactive material at the bone defect site is a valuable strategy to provide temporary mechanical support to the host tissue and promote bone healing and regeneration [2]. The term “bioactivity” traditionally refers to the capability of some special biomaterials, such as bioactive glasses, glass-ceramics and ceramics, to (i) chemically bond to bone and collagenous tissues forming a tight interface [3,4] and (ii) stimulate bone cells through specific regeneration paths via the release of osteo-stimulatory ionic dissolution products [5,6].

Bioactive glasses, glass-ceramics and ceramics are often produced as porous templates, i.e. scaffolds, which are able to support and guide the growth of new tissue in three dimensions (3D) allowing cell colonization, fluid permeation and vascularization [7,8].

Over the years, scientists identified a set of basic requirements that a scaffold for bone tissue engineering applications should typically exhibit, including porosity above 50 vol.%, pore sizes in the range of 100 to 500  $\mu\text{m}$ , and high interconnectivity of the pores [9]; furthermore, their compressive strength is recommended to be at least 2 MPa [10] and the scaffold degradation rate should match the kinetics of bone ingrowth [11]. These physical-mechanical properties are obviously in line with those of human cancellous bone [12,13], but the list is not exhaustive and the ranges for the different parameters are in principle quite broad.

Total porosity and mean pore size (or distribution) are relatively easy to determine and, very often, still are the characteristic parameters used to evaluate the potential suitability of new scaffolds for bone applications and/or compare different scaffold types. On the other hand, there is convincing evidence

that only porosity and pore size cannot describe a macroporous scaffold precisely enough for application in tissue engineering, but can just provide a preliminary assessment of its suitability. In this regard, Hollister et al. [14] reported no statistically significant difference in terms of regenerated bone volume within poly(propylene fumarate)/tricalcium phosphate (TCP) composite scaffolds with porosity of 30, 50 or 70 vol.%, which disagrees with the general idea of higher values of porosity promoting more bone tissue ingrowth [15]. Moreover, the same research group reported that differences in pore size had almost no influence on the rate of bone regeneration using polycaprolactone scaffolds with pores ranging within 350-800  $\mu\text{m}$  [16]. These discrepancies and even conflicting results among the studies are due to the complexity and interdependency of scaffold microstructural features and their mutual effect on the bone regeneration process [17], along with the inherent differences of the scaffold materials (e.g. inert polymer vs. osteoinductive TCP).

In order to partially overcome these limitations, Falvo D'Urso Labate et al. [18] proposed the use of a multiparametric score accounting for a combination of six microstructural parameters (total porosity, pore interconnectivity, pore size distribution, specific surface area, connectivity density and degree of anisotropy) in the attempt of achieving a more reliable comparison between ceramic scaffolds and trabecular bone; here, the use of micro-computed tomography ( $\mu\text{-CT}$ ) allowed an accurate estimation of the microstructural parameters.

Intrinsic permeability has been suggested as a key parameter to characterize scaffold architecture and mass transport properties as they are strongly related to bone growth and regeneration. In general, permeability quantifies the ability of a porous material to conduct fluid flow and relies on a combination of porosity, pore size, pore orientation, tortuosity and interconnectivity. The methods used to measure the intrinsic permeability of tissue engineering scaffolds have been comprehensively reviewed by Pennella et al. [19] in 2013 and are essentially based on the implementation of Darcy's law. An ASTM standard published in 2014 describes the procedures to follow in order to obtain a mean value of Darcy's

coefficient for tissue engineering porous scaffolds, which provides a measure of the permeability of the structure to fluid flowing through it that is driven by a pressure gradient created across it [20]. However, this approach requires the use of three transducers to assess upstream and downstream pressures and flow rate and may be contraindicated for highly brittle and/or resorbable scaffolds, which could be damaged by the fluid flow during the measurement execution.

This work proposes the assessment of the intrinsic permeability of bioactive silicate glass-ceramic scaffolds by an accurate acoustic method, which was first applied to commercial calcium carbonate porous structures in a previous work [21], in combination with non-destructive tomographic analysis. The relationship between intrinsic permeability and sintering temperature was investigated and the experimental results, supported by the data from  $\mu$ -CT, were aggregated within a theoretical model for a detailed characterization of the overall scaffold microstructure. To the best of the authors' knowledge, it is the first time that such a synergistic combination of reliable experimental measurements and  $\mu$ -CT-based analysis is reported in the field.

## **2. Materials and methods**

### **2.1. Preparation of samples**

#### *2.1.1. Glass production*

A six-oxide silica-based bioactive glass, named 47.5B, with nominal composition  $47.5\text{SiO}_2\text{-}2.5\text{P}_2\text{O}_5\text{-}20\text{CaO-}10\text{MgO-}10\text{Na}_2\text{O-}10\text{K}_2\text{O}$  (mol.%), was produced by traditional melt-quenching route, as described in previous works [22-24].

A glass frit was obtained by casting the melt into distilled water. Afterwards, the frit was milled (Pulverisette 0, Fritsch, Idar-Oberstein, Germany) and sieved (stainless steel sieves, Giuliani Technology Srl, Turin, Italy) in order to obtain a fine glass powder, with a grain size below  $32\text{ }\mu\text{m}$ .

### 2.1.2. Scaffold manufacturing by foam replication

Scaffolds were produced by foam replication technique, which was implemented for the first time in the biomedical field by Chen et al. for the production of 45S5 Bioglass®-based scaffolds [25].

In the present work, industrial polyurethane (PU) foam sheets (45 ppi) with a 10 mm thickness were used as sacrificial templates. The sintering temperature  $T_s$  ranged within 600-850°C.

In order to obtain a cylindrical geometry of the scaffolds, the foams were properly shaped by mean of cutting dies having a diameter of 13 or 16 mm. Sponges with smaller diameter were used to produce scaffolds sintered at 600 and 650 °C, for which the shrinkage upon sintering was reported to be lower than 5% [26].

Given that the scaffolds sintered above 650 °C underwent higher densification, it was necessary to use oversized sacrificial templates. This trick allowed us to maintain the final diameter of all the sintered samples in the optimal 8-10 mm range, thus matching the dimension of the sample holder used later for permeability measurements.

The glass slurry (H<sub>2</sub>O: poly(vinyl alcohol) (PVA): 47.5B powder = 64 : 30 : 6, wt.%) was prepared by suspending glass powder into a binder solution, according to the procedure described in our previous work [22]. Briefly, PVA granules were dissolved in water at 60 °C under continuous stirring (200 rpm), until a clear solution was obtained. Afterwards, some water was added dropwise to restore the original H<sub>2</sub>O/PVA ratio and the solution was left to cool at room temperature. Glass powders were then added and the slurry was mixed for 10 min to achieve a homogeneous dispersion of glass particles.

Subsequently, PU cylinders were dipped one-by-one for 15 s into the glass slurry. In order to remove the excess slurry from the pores, the cylinders were placed onto a raised metallic grid and subjected to a properly designed compression protocol, as depicted in Figure 1, aimed at improving the quality of the final scaffolds by controlling the slurry distribution, thus increasing the reproducibility and the repeatability of the manufacturing method.



All the samples underwent 3 complete immersion-compression cycles and were eventually left to dry at room temperature overnight on non-absorbent paper sheets.

Glass-coated foams (“greens”) were then thermally treated for 3 h at six different temperatures ( $T_{s1}=600$ ,  $T_{s2}=650$ ,  $T_{s3}=700$ ,  $T_{s4}=750$ ,  $T_{s5}=800$  and  $T_{s6}=850$ , °C), selected on the basis of previous thermal analyses [27]) with a constant heating and cooling rate of 5 °C/min and 10 °C/min, respectively, in order to selectively investigate the effect of the sintering treatment on the scaffold microstructural features.

In order to obtain samples with suitable dimensions for permeability assessment (section 2.2.2), a metallographic grinding polishing machine (Struers, LaboPol-2, 250-500 rpm) and SiC sand papers (#600 and #800) were used to rectify the upper and lower surfaces of the samples so that flat and parallel faces were obtained. After polishing, scaffolds were immersed in an ultrasonic bath for 5 min to remove polishing debris and left to dry at room temperature overnight.

Final dimensions (diameter,  $D_s$  and length,  $L_s$ ) and mass  $m_s$  of the scaffolds after polishing were determined by digital caliper and precision scale, respectively.

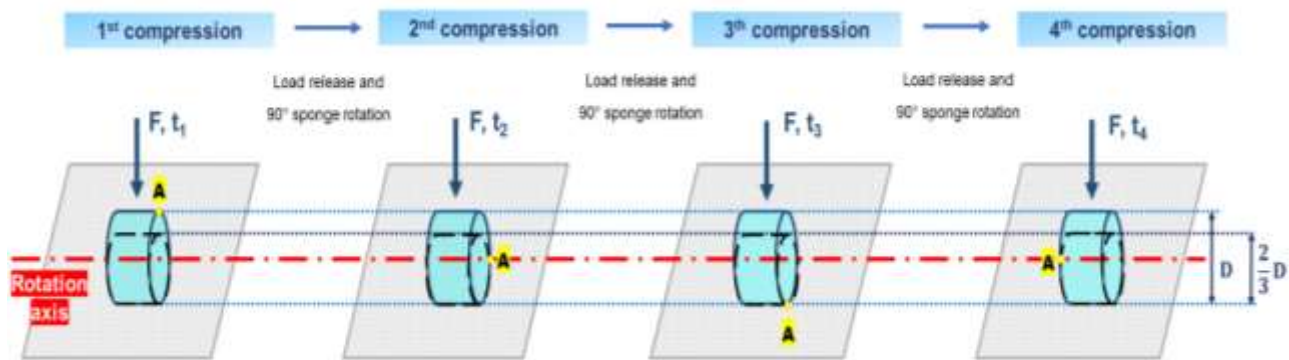


**Figure 1.** Schematic representation of the compression protocol followed for scaffold manufacturing.

After each immersion, the cylindric sample was placed onto a raised metallic grid and compressed to 2/3 of its diameter by the application of an instantaneous load ( $F=8.829$  N), perpendicular to the grid plane.

In total, each sample underwent 4 compressions; between a compression and the following one, the

cylinder was rotated 90° around the rotation axis in order to achieve a homogeneous distribution of the glass slurry within the porous structure. The path followed by point “A” in the picture indicates the direction of rotation of the cylinder.

## 2.2. Characterization of scaffolds

### 2.2.1. Theoretical background: constitutive equation and model development

Since Reynolds theory [28], Forchheimer equation [29] is commonly used to describe the pressure loss of a one-directional fluid flow through a permeable material, as the sum of a viscous energy loss term, proportional to the linear flow velocity  $U$ , and an inertial loss term, proportional to the velocity squared  $U^2$ , according to Equation 1:

$$-\frac{\partial P}{\partial x} = \mu a U + \rho b U^2 \quad (1)$$

where  $x$  is the flow direction,  $\partial P$  is the pressure gradient, and  $a$  and  $b$  are two empirical parameters related to the fluid dynamic viscosity  $\mu$  and the fluid density  $\rho$ , respectively.

The constitutive equation here proposed relies on the Ergun equation [30] revised by Niven [31], in which the characteristic length scale of the internal structure of the porous medium is assumed as the average pore diameter  $d_p$ , according to [32,33], for pores of any arbitrary shape [34,35], and on the recent Wu-Yu-Yun resistance model [36]. The two empirical constants  $a$  and  $b$  of the Forchheimer equation are thus replaced by two pore morphology-dependent expressions (Equation 2 and 3) with a well-defined physical meaning:

$$a = 72\tau \frac{(1-\varepsilon)^2}{\varepsilon^3} \cdot \frac{1}{\varphi_p^2 d_p^2} \quad (2)$$

$$b = 0.75\tau \frac{(1-\varepsilon)}{\varepsilon^3} \cdot \frac{1}{\varphi_p d_p} \cdot \left( \frac{3}{2} + \frac{1}{\beta^4} - \frac{5}{2\beta^2} \right) \quad (3)$$

where  $d_p$  is the average pore diameter,  $\varphi_p$  is the pore shape factor (sphericity),  $\varepsilon$  is the effective porosity,  $\tau$  is the pore tortuosity and  $\beta$  is the ratio of  $d_p$  to throat diameter  $d_t$ .

The pores diameter of arbitrary shape,  $d_p$  is calculated according to [31], from Equation 4:

$$d_p = \frac{6V_p}{A_p \varphi_p} \quad (4)$$

where  $V_p$  is the volume of a single (non-spherical) pore and  $A_p$  is its surface area.

The pore sphericity  $\varphi_p$  is the measure of how closely the shape of a pore resembles that of a perfect sphere and it is defined as the ratio of the maximum radius of the sphere inscribed in the pore of any arbitrary shape, and the minimum radius of the sphere circumscribed in the same pore [35].

The effective porosity  $\varepsilon$  is defined as the fractional volume of the pores that actually allow fluid flow within the permeable material, without accounting for voids of dead-end pores and closed pores,  $\varepsilon_c$ ; it is different from the total porosity  $\varepsilon_0$ , defined as the percentage of total void space within the volume of the permeable medium, regardless of the pore void interconnections. Namely,  $\varepsilon$  is given by Equation 5:

$$\varepsilon = \varepsilon_0 - \varepsilon_c \quad (5)$$

The  $\beta$  parameter, defined as the ratio of  $d_p$  to  $d_t$ , i.e.  $\beta = d_p/d_t$ , where the throat size  $d_t$  is assumed as the average diameter of throats [36,37], is related to the effects of contracting and expanding pore cross-sections, and is expressed as function of  $\varepsilon$ , according to Equation 6:

$$\beta = \frac{1}{1-\sqrt{1-\varepsilon}} \quad (6)$$

The pore morphology, in terms of sphericity and average pore cross-section changes, perpendicularly to the direction of fluid flow, are schematically depicted in Figure 2.

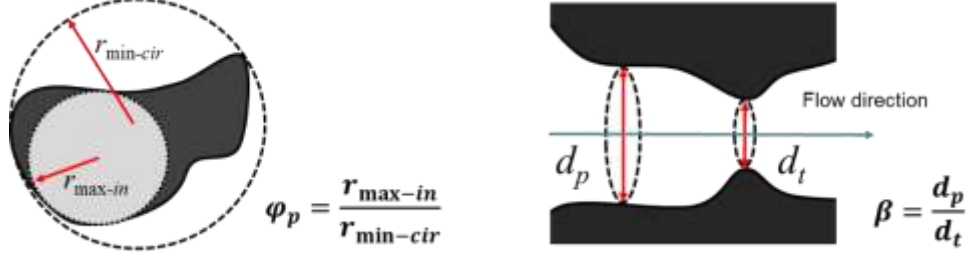


**Figure 2.** The pore sphericity and the pore cross-section change, due to a throat, in the flow direction.

The tortuosity  $\tau$ , defined as the ratio between the length  $L_s$  of the permeable medium (scaffold), along the macroscopic pressure gradient in the  $x$ -direction, and the actual length  $L_p$  of the tortuous pore, i.e.  $\tau = L_p/L_s$ , can be estimated from the comprehensive Yu and Li's geometrical model [38] according to Equation 7:

$$\tau = \frac{1}{2} \left[ 1 + \frac{1}{2} \sqrt{1 - \varepsilon} + \sqrt{1 - \varepsilon} \frac{\sqrt{\left(\frac{1}{\sqrt{1 - \varepsilon}} - 1\right)^2 + \frac{1}{4}}}{1 - \sqrt{1 - \varepsilon}} \right] \quad (7)$$

This relation is considered representative enough of tortuosity in porous media, although derived from a geometrical approximation, and it is consistent with other studies [39,40].

By explicating the correct relationships among terms, the pressure loss is given by Equation 8:

$$-\frac{\partial P}{\partial x} = \mu \left[ 72\tau \frac{(1 - \varepsilon)^2}{\varepsilon^3} \cdot \frac{1}{\varphi_p^2 d_p^2} \right] U + \rho \left[ 0.75\tau \frac{(1 - \varepsilon)}{\varepsilon^3} \cdot \frac{1}{\varphi_p d_p} \cdot \left( \frac{3}{2} + \frac{1}{\beta^4} - \frac{5}{2\beta^2} \right) \right] U^2 \quad (8)$$

The constitutive equation, in this form, is intended only for gas-flow through stiff solid permeable materials.

At the macroscale level for laminar flow, Darcy transport model describes the flow of a fluid through a permeable material as a proportional relation between the fluid velocity and the pressure drop gradient (Equation 9):

$$-\frac{\partial P}{\partial x} = \frac{\mu}{k} U \quad (9)$$

where  $k$  is the intrinsic permeability.

By combining Equation 1, with the above defined parameters, and Equation 9 a relationship with the intrinsic permeability  $k$ , can be found (Equation 10):

$$\frac{\mu}{k} U = \mu a U + \rho b U^2 \quad (10)$$

It has been demonstrated that, if  $U$  is low, the inertial losses dependent on  $U^2$  (Equation 10) can be considered negligible [33]. This condition is satisfied when the interstitial Reynolds number  $R_i$  is close to unity. The interstitial Reynolds number is given by Equation 11:

$$R_i = \frac{\rho d_p U \phi_p}{\mu (1-\varepsilon)} \quad (11)$$

Under the assumption that  $R_i < 1$  and then  $\rho b U^2 / \mu a U < 0.01$ , the intrinsic permeability  $k$  of a permeable material (scaffold) can be determined in the linear Darcy's region by Equation 12:

$$k = \frac{\mu U}{\mu a U + \rho b U^2} \cong \frac{1}{a} \quad (12)$$

By combining Equation 12 and Equation 2, the intrinsic permeability  $k$ , can be expressed as a function of pores morphology only, as described by Equation 13:

$$k \cong \frac{\phi_p^2 d_p^2}{72\tau} \cdot \frac{\varepsilon^3}{(1-\varepsilon)^2} \quad (13)$$

### 2.2.2. Intrinsic permeability measurements: the experimental set-up

In practice, when the interstitial Reynolds number  $R_i$  is lower than 8.6, the fluid flow through the permeable material is considered laminar (with non-linear effects below 10%) [19, 33] and the intrinsic permeability  $k$  can be determined, in the Darcy's linear region, by measuring the volumetric flow rate and the pressure loss through a permeable sample, as described by Equation 14:

$$k = \mu \frac{Q_v}{\Delta P} \cdot \frac{L_s}{A_s} \quad (14)$$

where  $\mu$  is the dynamic fluid viscosity,  $Q_v$  is the volumetric flow rate ( $Q_v = U \cdot A_s$ ),  $\Delta P$  is the pressure differential upstream and downstream the permeable material along the length  $L_s$  of the sample, and  $A_s$  is the surface area of the sample perpendicular to the flow direction.

The experimental technique here implemented is based on the generation of a slow alternating airflow through the permeable sample; the resulting sinusoidal pressure component drop is accurately measured by means of a low-frequency pressure field microphone. The permeability  $k$  is determined on the basis of the ratio between the r.m.s. volumetric airflow rate and the r.m.s. pressure, according to Darcy's law (Equation 15):

$$k = \mu \frac{q_{v,rms}}{p_{rms}} \cdot \frac{L_s}{A_s} \quad (15)$$

The alternating r.m.s. volumetric airflow  $q_{v,rms} = \pi f h A_k (\sqrt{2})^{-1}$  depends on the surface area  $A_k$  of the piston, the peak-to-peak piston stroke  $h$  and the imposed frequency of oscillation  $f$ ; the sinusoidal r.m.s. pressure component  $p_{rms} = 1.4 p_0 \partial V (V_0 \sqrt{2})^{-1}$  depends on the atmospheric static pressure  $p_0$  and the sinusoidal volume variation  $\partial V$ , which is induced by the motion of the piston on the volume of air  $V_0$  closed between the permeable sample and the piston. The dynamic viscosity  $\mu$  of the air, for acoustic applications, is calculated on the basis of environmental air temperature  $T_{air}$  and relative humidity  $RH$  during the measurements by applying Rasmussen model [41]. By using a very low frequency of oscillation, namely

$f=0.15$  Hz, and considering the geometry of the measurement system (piston surface area  $A_k=1.9 \cdot 10^{-3} \text{ m}^2$  and piston stroke  $h=1.7 \cdot 10^{-3} \text{ m}$ ), the alternating volumetric airflow rate was  $q_{v,r.m.s}=1.09 \cdot 10^{-6} \text{ m}^3/\text{s}$ .

The detailed description of the measurement device and experimental procedure (applied to porous calcite bioceramics) is available in [21] and a schematic representation of the principle of measurement is depicted in Figure 3.

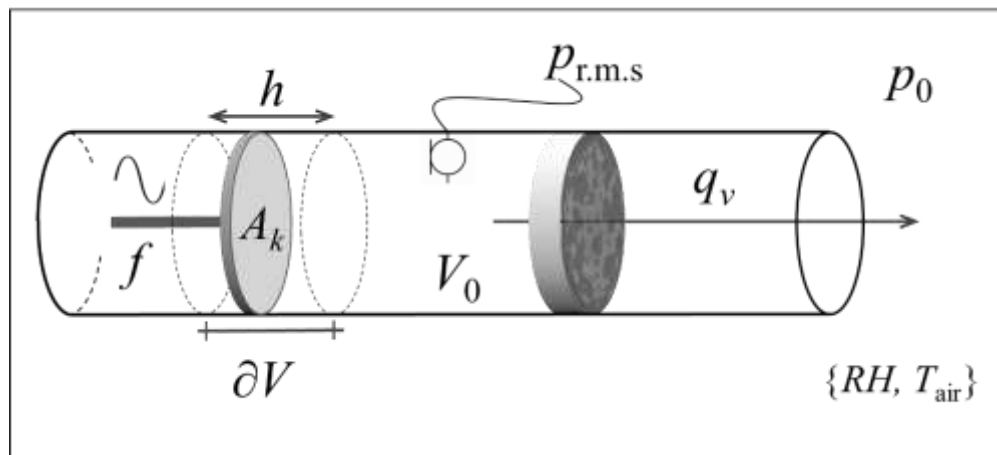


**Figure 3.** The principle of intrinsic permeability measurement by using an alternating airflow.

### 2.2.3. Morphological and microstructural assessment

The total porosity  $\varepsilon_0$  of the scaffolds was calculated in quadruplicate by gravimetric method, according to Equation 16 [15]:

$$\varepsilon_0 = (1 - \rho_{app}/\rho_{glass}) \quad (16)$$

where  $\varepsilon_0$  is the total porosity,  $\rho_{app}$  is the apparent density of the scaffold (calculated as mass-to-volume ratio), and  $\rho_{glass}$  is the density of 47.5B bioactive glass ( $2.64 \text{ g/cm}^3$ ), assessed by Archimedes Principle in a previous study [42]. Total porosity results were expressed as mean value  $\pm$  standard deviation.

Morphological features of the scaffolds were investigated by scanning electron microscopy (SEM) (field-emission SEM equipped with EDS; Supra<sup>TM</sup> 40, Zeiss, Oberkochen, Germany), using an inspection voltage of 15 kV. Before the analysis, a conductive layer of chromium ( $\approx 7$  nm) was sputtered on the surface of the scaffolds.

#### 2.2.4. $\mu$ -CT analysis: average pore diameter, sphericity assessment and pore interconnectivity

X-ray  $\mu$ -CT scanning of the glass scaffolds was performed in air by a Phoenix Nanotom S (Waygate Technologies / General Electric Sensing and Inspection Technologies GmbH, Wunstorf, Germany). Projection images were collected using a source voltage of 110 kV and a source current of 110  $\mu$ A, with no X-ray filters employed. In order to avoid any mismatching between the 0° and the 360° shadow images in case of a slight movement of the sample during the data collection, a translational motion compensation was used. A 10-fold magnification was used with a voxel size of 5.00  $\mu$ m. Rotation step size was 0.50°, exposure time 1.5 s and tube mode 0. Mode 0 is one of the four specific modes of the instrument, the so-called power mode with maximum target power 2.7 W, whereas modes 1, 2 and 3 are nanofocus modes with lower maximum target power. Three images were integrated for each rotation step and one blank image was collected prior to acquisition of these three images. Virtual volumes were reconstructed from the projection images using the datos-x reconstruction software provided by the equipment manufacturer. The structural features of the scaffolds were determined by using the VGStudio Max 3.3 software (Volume Graphics, Heidelberg, Germany) based on the Cauchy-Crofton approach, through the add-on modules Coordinate Measurement and Foam/Powder Analysis. A virtual cylinder was fitted into each reconstructed scaffold model and the cylinder size maximized without extending out of the scaffold contours. The cylinder was extracted as a separate virtual volume and a 3×3×3 median filter was applied to the data for de-noising before an isovalue-based surface determination procedure was run. The Foam/Powder analysis module was used to extract foam structure data employing a merge



threshold of 95% and a standard precision procedure. The module allows the segmentation of CT data into topologically disconnected components which can be visualized and statistically analysed. Information on number of pores, on pore shape and size (surface area  $A_p$ , volume  $V_p$ , sphericity  $\phi_p = A_{sphere}/A_p$ ) as well as on pore interconnectivity (open, closed, border) were collected and used for calculations.

### 2.2.5. Determination of the effective porosity and tortuosity

On the basis of the accurate experimental data obtained from  $\mu$ -CT analysis (pore average diameter  $d_p$ , sphericity  $\phi_p$ ) and from the measurement of intrinsic permeability  $k$ , it was possible to define the overall microstructural properties as a function of effective porosity  $\varepsilon$  by applying Equation 13 to each scaffold. According to Equation 7, pore tortuosity only depends on the effective porosity; thus, after substitution in Equation 13, the Equation 17 is obtained:

$$\frac{72k}{\phi_p^2 d_p^2} = \frac{\varepsilon^3}{(1-\varepsilon)^2} \cdot \left[ \frac{1}{2} \cdot \left( 1 + \frac{1}{2} \cdot \sqrt{1-\varepsilon} + \sqrt{1-\varepsilon} \cdot \frac{\sqrt{\left(\frac{1}{\sqrt{1-\varepsilon}}-1\right)^2 + \frac{1}{4}}}{1-\sqrt{1-\varepsilon}} \right) \right]^{-1} \quad (17)$$

The only unknown parameter was the effective porosity  $\varepsilon$ , calculated using an online available graphic calculator (GeoGebra) from the zero-values of the function of Equation 17.

Once the effective porosity  $\varepsilon$  was determined, the full set of microstructural parameters could be calculated, too, including the fraction of non-interconnected pores  $\varepsilon_c$  within the scaffolds (Equation 5), as well as the ratio of pore diameter to throat diameter  $\beta$  (Equation 6), the pore tortuosity  $\tau$  (Equation 7), and the actual length  $L_p$  of the tortuous pore ( $L_p = \tau \cdot L_s$ ). Moreover, the actual interstitial Reynolds number  $R_i$ , the viscous loss term  $a\mu U$  and inertial loss term  $b\rho U^2$  could be

definitively quantified. Assuming laminar flow conditions, the friction factor  $f_c$  was determined by Equation 18 [43]:

$$f_c = 72 \tau / R_i + 0.75 \tau \quad (18)$$

As a consequence, an estimation of the permeability  $k$  as a function of both viscous and inertial effects was achieved.

#### 2.2.6. Statistical methods

Scaffold diameter  $D_s$ , height  $L_s$ , surface area  $A_s$  and volume  $V_s$ , were expressed as mean value  $\pm$  standard deviation, obtained from 12 independent measurements for each sintering group.

The intrinsic permeability  $k$  was determined in quadruplicate for each sintering group. Results of permeability were expressed in the range between the 1<sup>st</sup> and the 3<sup>rd</sup> quartile.

Analogously, average pore diameter and related data dispersion were expressed in the range defined by the 1<sup>st</sup> and the 3<sup>rd</sup> quartile. Besides, a careful selection of outliers was carried out by using the Chauvenet's criterion: any values that fall outside the probability band  $P=1-(1/2n)$  centered on the mean value of the  $n$ -size sample, was excluded.

Two reasons for data exclusion were supposed: i) unexpected damages or breakage of the pore walls due to the inherent brittleness of the glassy material and ii) possible misinterpretations of the  $\mu$ -CT image processing.

### 3. Results

#### 3.1. Total porosity, morphological and geometrical features

Table 1 collects the general macro-scale features of foam-replicated scaffolds sintered at different temperatures, including primary and derived geometrical dimensions (diameter  $D_s$ , height  $L_s$ , volume  $V_s$ , cross-sectional area  $A_s$ ), apparent density  $\rho_{app}$  and total porosity  $\varepsilon_0$ , calculated according to Equation 16.

**Table 1.** Geometrical dimensions, physical and structural properties of 47.5B scaffolds sintered at different temperatures, expressed as mean value  $\pm$  standard deviation.

	Sintering Temperature /°C					
	600	650	700	750	800	850
$D_s$ / mm	8.3 $\pm$ 0.3	8.2 $\pm$ 0.6	10.3 $\pm$ 0.5	10.7 $\pm$ 1.0	10.7 $\pm$ 0.6	11.0 $\pm$ 0.6
$L_s$ / mm	7.1 $\pm$ 0.7	6.7 $\pm$ 0.6	8.1 $\pm$ 0.5	6.7 $\pm$ 0.3	6.9 $\pm$ 0.1	6.1 $\pm$ 0.4
$A_s$ / mm <sup>2</sup>	54.6 $\pm$ 4.5	53.3 $\pm$ 7.5	82.8 $\pm$ 8.2	90.4 $\pm$ 17.0	90.6 $\pm$ 11.0	94.5 $\pm$ 11.0
$V_s$ / mm <sup>3</sup>	389.0 $\pm$ 66.0	355.2 $\pm$ 77.0	670.0 $\pm$ 100.0	607.9 $\pm$ 140.0	624.3 $\pm$ 84.0	577.2 $\pm$ 100.0
$\rho_{app}$ / g/cm <sup>3</sup>	0.68 $\pm$ 0.10	0.78 $\pm$ 0.04	0.42 $\pm$ 0.01	0.69 $\pm$ 0.04	0.66 $\pm$ 0.05	1.18 $\pm$ 0.05
$\varepsilon_0$	0.79 $\pm$ 0.03	0.71 $\pm$ 0.01	0.84 $\pm$ 0.00	0.74 $\pm$ 0.02	0.75 $\pm$ 0.02	0.55 $\pm$ 0.02

The total porosity of all the scaffolds produced varied between 55 and 84 vol.%: these values definitely lie in the range of human trabecular bone and satisfy the minimum bone tissue engineering (BTE) requirements for allowing proper cell infiltration, attachment and new tissue growth [7, 44-46]. However, no clear trend was observed as a function of the sintering temperature.

SEM morphological analyses revealed that all the scaffold exhibited a sponge-like 3D architecture, inherited from PU industrial foams used as sacrificial templates (Figure 4).

However, some differences derived from the thermal treatment could be pointed out. In particular, scaffolds sintered at lower temperatures exhibited the typical open-cell trabecular morphology of glass-based scaffolds produced by foam replica method [25,47,48], which is very similar to that of human spongy bone [49], with pore size ranging between 200-500  $\mu$ m and trabecular thickness defined between 70 and 100  $\mu$ m. Such a typical morphology was observed only up to 700 °C, which corresponded approximately to the temperature of crystallization onset ( $T_x$ ) of 47.5B glass, as reported by Fiume et al. in a previous study [27].

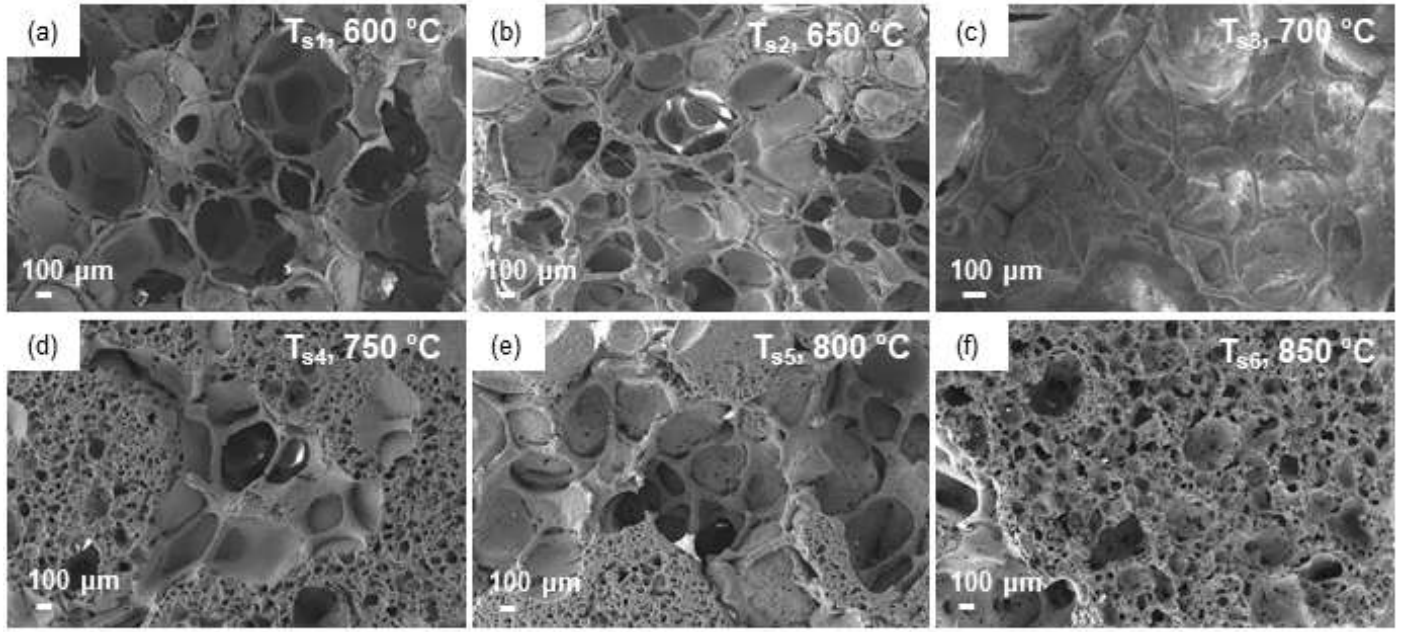


**Figure 4.** SEM images of 47.5B-based scaffolds produced by replication of commercial PU sponges.

Changes in morphology due to the variation in the sintering temperature can be clearly appreciated.

Just after crystallization (Figure 4d-e), indeed, a double distribution of pore size was observed, with larger pores, defined by trabeculae, ranging between 200  $\mu\text{m}$  and 500  $\mu\text{m}$ , and smaller ones even below 50  $\mu\text{m}$ .

Once glass crystallization was completed ( $T_s \geq 800^\circ\text{C}$ ), a consistent drop in  $\varepsilon_0$  was observed (Table 1) along with more homogeneous pore size and distribution: Figure 4f shows that pores with size of about 100-150  $\mu\text{m}$  were preponderant, while the number of bigger pores, reaching 300-400  $\mu\text{m}$ , was remarkably lower.

Scaffold surface topography was then investigated at higher magnification in correspondence of 3 significant temperatures, according to previous assessments regarding the thermal behavior of the glass [27]. i.e. before crystallization ( $T_{s1}=600^\circ\text{C}$ ), at the crystallization onset ( $T_{s3}\sim T_x=700^\circ\text{C}$ ) and at the end of the crystallization process ( $T_{s6}=T_f=850^\circ\text{C}$ ).

As displayed in Figure 5a, the surface of the scaffold heat-treated at 600 °C appeared smooth and topographically homogeneous, thus exhibiting the typical features of an amorphous material (glass). At higher magnifications (Figure 5b), sintering necks between adjacent glass particles and interstitial pores resulting from the thermal treatment can also be observed.

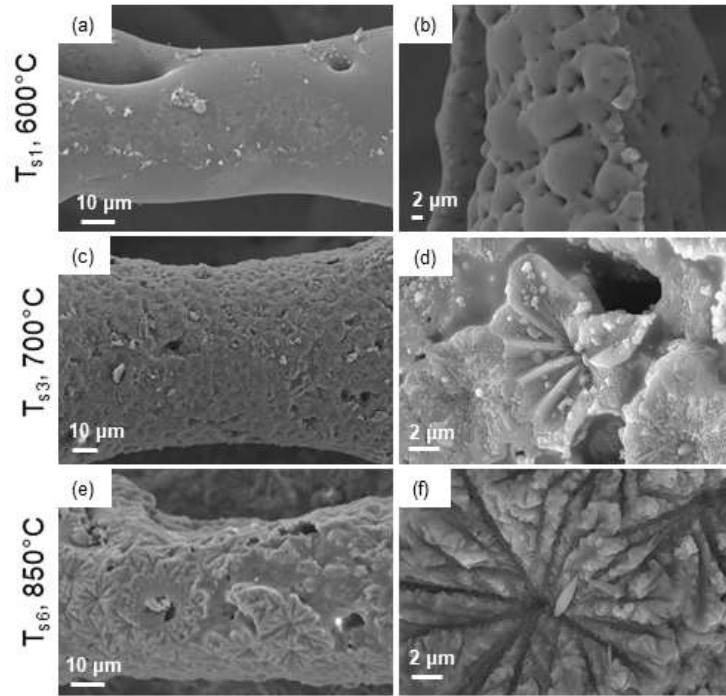


**Figure 5.** SEM images of 47.5B scaffold surfaces at different magnification sintered at 600°C (a-b), 700°C (c-d) and 850°C (e-f). Material devitrification resulted in the formation of flower-like crystals associated to the nucleation of combeite.

Approaching the crystallization temperature, evidence of the system devitrification appeared on the scaffold surface. At 700 °C, indeed, flower-like crystals in the range of 10-12 μm were observed, surrounded by the glassy amorphous matrix (Figure 5c-d).

At 850°C, the surface of the scaffold was completely covered by these crystals (Figure 5e), which became gradually bigger and more defined in shape (Figure 5f), as a result of the growth process of crystalline phases upon sintering treatment at high temperature.

Consistently with what reported in our previous studies on the same glass composition [22,23,27], the observed crystals were associated to the development of a single crystalline phase, identified as combeite  $\text{Na}_2\text{Ca}_2(\text{Si}_3\text{O}_9)$ , which is highly biocompatible and is also the main phase found in crystallized 45S5 Bioglass® [50].

### 3.2. Average pore diameter

The pore diameter  $d_p$  of each single arbitrarily-shaped pore was calculated according to Equation 4 by making use of the data from  $\mu$ -CT topographic analysis (Figure 6), including the given non-spherical volume  $V_p$ , surface area  $A_p$  and pore shape factor  $\phi_p$  (sphericity). Pore interconnectivity, provided as output by the software used for  $\mu$ -CT data analysis (VGStudioMax) allowed us to detect closed pores and exclude them from the analysis.

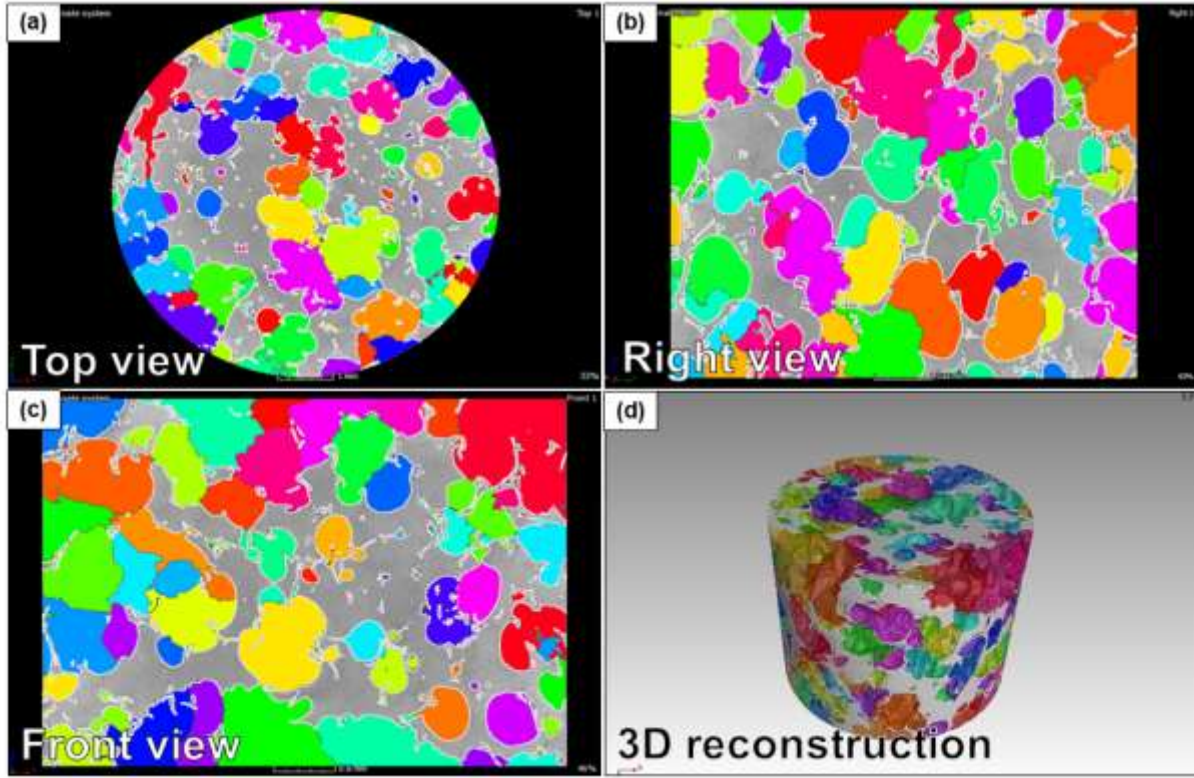


**Figure 6.** Example of  $\mu$ -CT images of foam-replicated cylindrical scaffolds: Top, right, front views and 3D reconstruction of a 47.5B-glass scaffold sintered at  $T_{sl}=600^{\circ}\text{C}$ ; merge threshold 95%.

The distribution of the overall pore diameter at each sintering temperature is graphically represented in Figure 7. Histograms revealed comparable results to SEM preliminary investigation: increasing the sintering temperature, pore size shifted towards lower values and the overall number of pores within the scaffold increased, consistently with what observed in Figure 4.

Statistical results of  $d_p$  analysis are summarized in Table 2. As it is possible to notice, the number of supposed outliers was  $\sim 1\%$  of the number of total pores analyzed, so it was considered negligible. The values of the median ( $d_p$ ) is close to the total average of the diameters  $\overline{d_p}$  within the limits of 1<sup>st</sup> and the 3<sup>rd</sup> quartile, and can be therefore considered a proper estimation of the pore average diameter  $d_p$  of



arbitrary shape. The values of average pore sphericity  $\bar{\varphi}_p$  and the related standard deviation  $\sigma_\varphi$  are also collected in Table 2.

**Table 2.** Pore diameter: experimental data and statistical results.

	Sintering Temperature /°C					
	600	650	700	750	800	850
<b>N. Pores</b>	730	199	1793	6601	9345	2434
<b>N. Outliers</b>	0	2	20	85	133	21
<b>Mean <math>\bar{d}_p</math> /mm</b>	0.67	0.78	0.33	0.30	0.26	0.22
<b><math>\sigma_d</math> / mm</b>	0.34	0.43	0.16	0.12	0.11	0.22
<b>Median (<math>d_p</math>) /mm</b>	0.68	0.78	0.33	0.30	0.26	0.22
<b>1<sup>st</sup> quartile /mm</b>	0.41	0.48	0.26	0.25	0.22	0.17
<b>3<sup>rd</sup> quartile /mm</b>	0.92	1.05	0.43	0.37	0.32	0.28
<b>Max <math>d_p</math> /mm</b>	1.68	1.94	1.03	0.92	0.82	0.91
<b>Min <math>d_p</math> /mm</b>	0.02	0.01	0.14	0.14	0.12	0.01
<b><math>\bar{\varphi}_p</math></b>	0.286	0.345	0.268	0.260	0.247	0.185
<b><math>\sigma_\varphi</math></b>	0.064	0.081	0.091	0.084	0.088	0.071

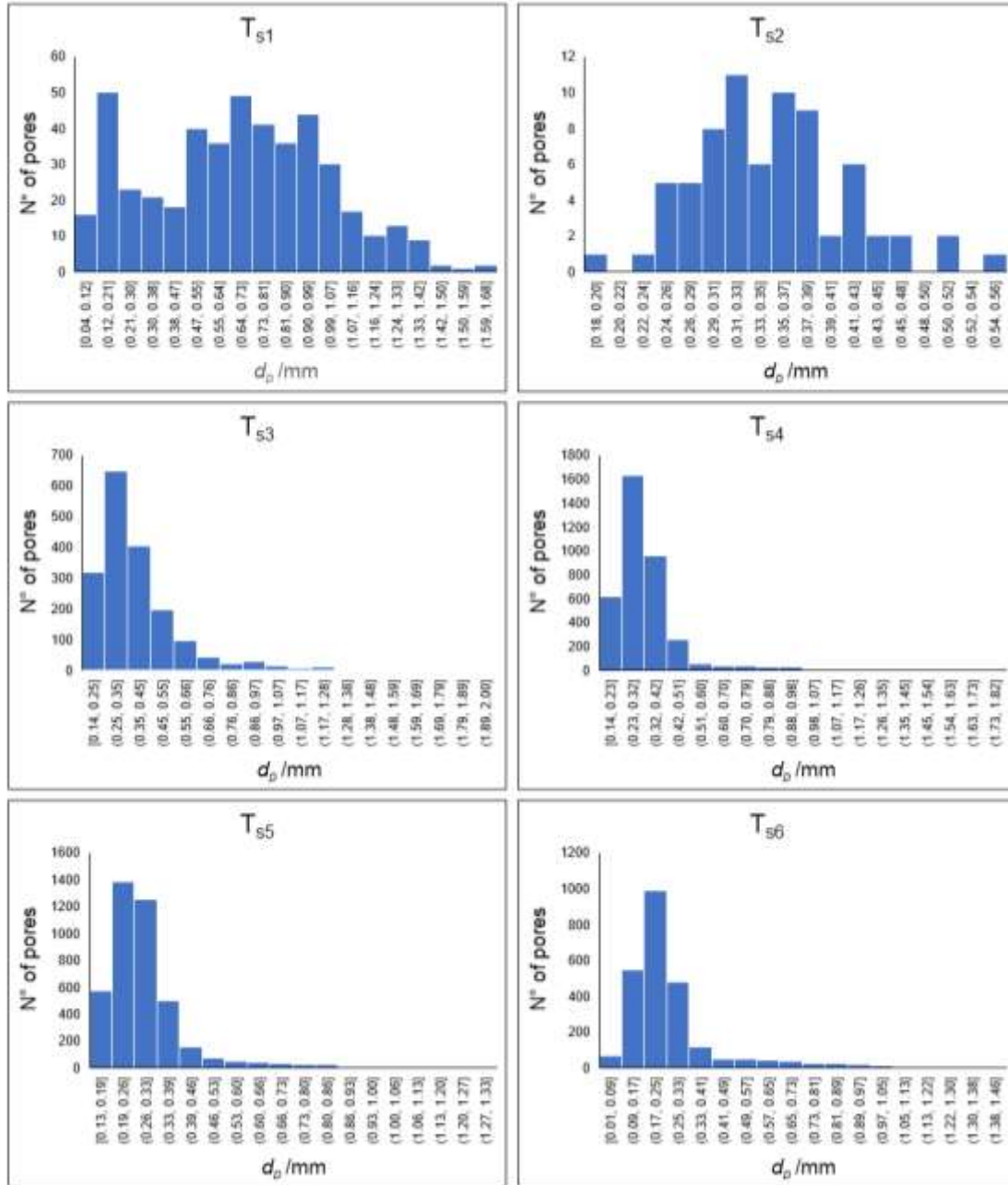


**Figure 7.** Actual distribution of pore diameters  $d_p$  within 47.5B scaffolds sintered at different temperatures. Each histogram represents the pore size distribution within a representative sample for each sintering group.

### 3.3. Intrinsic permeability $k$

The intrinsic permeability  $k$  of each sample was determined from the measurements of alternating airflow pressure drop; through a cylindrical sample of  $\sim 9\text{-}10\text{ mm}$   $D_s$ , the resulting value of the linear airflow velocity was  $U \sim 1.2 \cdot 10^{-2}\text{ m/s}$ . Thus, the value of the airflow velocity was low enough to maintain a laminar flow through the permeable sample, since the interstitial Reynolds number was  $\sim 1$  (Equation 11) and, therefore, by imposing these boundary conditions, the intrinsic permeability  $k$  was determined with an error due to the inertial effects of about 1%.

Experimental data obtained for each sintering group are shown in Table 3. Decreasing permeability values were observed with the increase of the  $T_s$ , following approximately a linear trend, discontinued by samples sintered at  $700\text{ }^\circ\text{C}$ , at which a pronounced permeability drop was observed.

**Table 3.** Intrinsic permeability experimental results and statistical analysis.

	Sintering Temperature $^\circ\text{C}$					
	600	650	700	750	800	850
$k / \cdot 10^{-10}\text{ m}^2$	2.49-2.81	2.59-2.85	1.10-1.29	1.42-1.70	1.03-1.16	0.04-0.06
<b>Max</b> $k / \cdot 10^{-10}\text{ m}^2$	3.04	2.95	1.35	1.72	1.30	0.08
<b>Min</b> $k / \cdot 10^{-10}\text{ m}^2$	2.08	2.54	0.96	1.39	0.81	0.02

### 3.4. Effective porosity and related parameters

Graphical solution of Equation (17) for the calculation of the effective porosity at each sintering temperature in the physically-meaningful range (0-1) is depicted in Figure 8. Analogously to what previously said for total porosity, no clear trend of effective porosity as a function of the sintering temperature was observed.

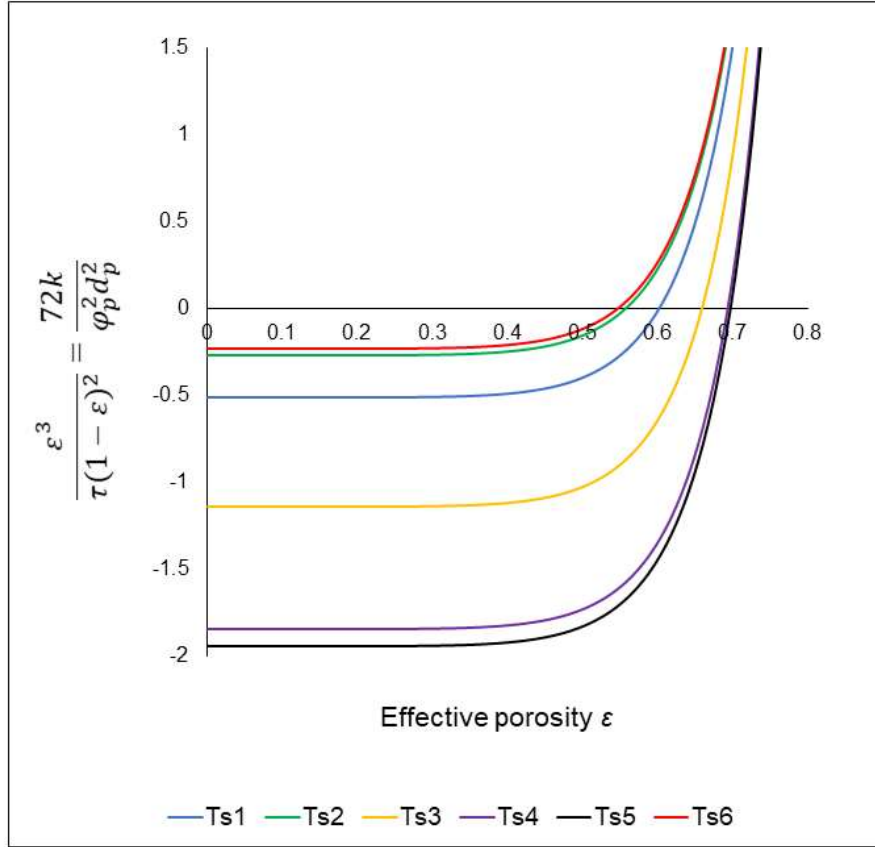


**Figure 8.** Graphical solutions of Equation 17, assessed by using experimental data of permeability  $k$  and average pore diameter  $d_p$ .

Figure 9 provides a picture of the overall microstructural features and permeability properties in relation with the DTA thermogram of 47.5B glass in the temperature range 600-850°C.

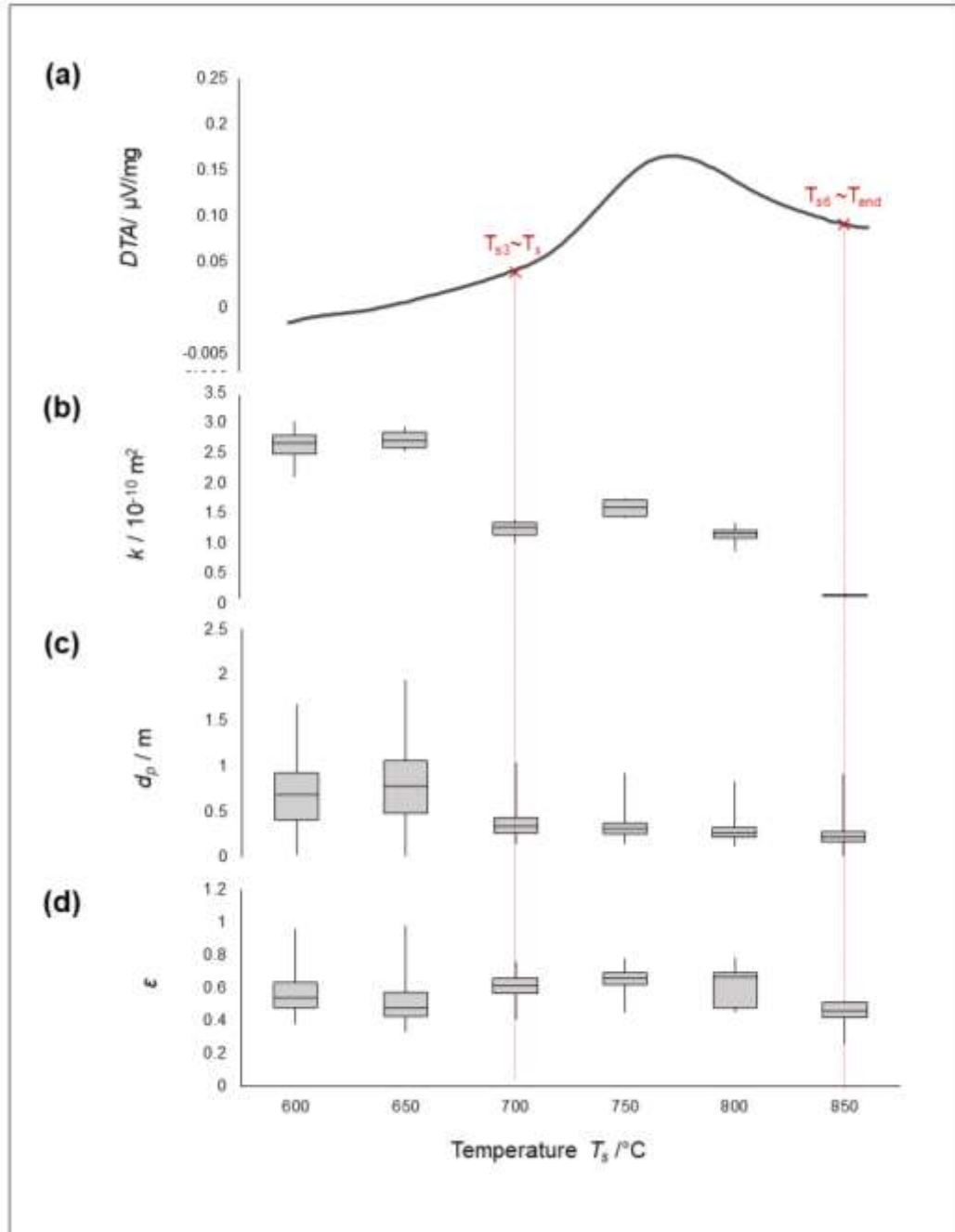


**Figure 9.** Thermal behaviour and microstructural properties of foam replicated scaffolds: (a) DTA thermogram showing the thermal behaviour of 47.5B bioactive glass in the range 600-850 °C [27]; (b) experimental intrinsic permeability data of the samples represented within the 1<sup>st</sup> and the 3<sup>rd</sup> quartile; (c) distributions of the diameter of pores in the samples represented within the 1<sup>st</sup> and the 3<sup>rd</sup> quartile; (d) distributions of the effective porosity of the samples represented within the 1<sup>st</sup> and the 3<sup>rd</sup> quartile.

Finally, the assessment of the effective porosity allowed achieving a comprehensive characterization of scaffold microstructure and mass transport properties, as summarized in Table 4.

**Table 4.** Microstructural and transport properties of scaffolds produced at different sintering temperatures.

	Sintering Temperature /°C					
	600	650	700	750	800	850
Effective porosity $\varepsilon$	0.54	0.48	0.61	0.66	0.66	0.46
Total porosity $\varepsilon_0$	0.75	0.71	0.84	0.74	0.75	0.55
Closed porosity $\varepsilon_c$	0.21	0.23	0.23	0.08	0.09	0.09
Open-to-close ratio $R$	2.57	2.09	2.65	8.25	7.33	5.11
Pore diameter/throat $\beta$	1.30	1.35	1.24	1.21	1.20	1.37
Tortuosity $\tau$	1.40	1.50	1.30	1.26	1.25	1.53
Sample length $L_S$ / m	0.007	0.007	0.008	0.007	0.007	0.006
Pore length $L_P$ / m	0.010	0.010	0.011	0.008	0.009	0.009
Reynolds num. $R_i$	0.56	0.71	0.20	0.18	0.15	0.06
Friction factor $f_c$	179.78	153.44	466.01	492.11	587.53	1882.28
$a\mu U$ /Pa·m <sup>1</sup>	1334.0	1379.3	1879.6	1348.6	1878.4	40846.8
$b\rho U^2$ /Pa·m <sup>1</sup>	2.9	4.4	1.2	0.7	0.8	11.8
Linearity deviation (%)	0.22	0.32	0.06	0.05	0.04	0.03
$k/\cdot 10^{-10}$ m <sup>2</sup>	2.679-2.802	2.633-2.811	1.277-1.291	1.636-1.650	0.245-1.166	0.051-0.052

#### 4. Discussion

In the present study, the effect of the sintering temperature on the microstructural properties of bioactive glass scaffolds was comprehensively investigated. The basic material for all the scaffolds was a bioactive six-oxide glass composition in the system SiO<sub>2</sub>-P<sub>2</sub>O<sub>5</sub>-CaO-MgO-Na<sub>2</sub>O-K<sub>2</sub>O, which was previously designed and characterized by our research group [26,27,51]. DTA analyses performed on the glass

revealed a workability window – i.e. the difference between the crystallization onset and the glass transition temperature - of  $\sim 200$  °C, thus allowing the production of mechanically resistant and highly bioactive synthetic glass-based bone grafts [27].

In addition, despite high sintering temperatures, leading to the development of crystalline phases, are usually associated to a decrease in the bioactive behaviour of the material, the composition used in the present study was demonstrated to retain hydroxyapatite-forming ability (i.e., bioactivity) up to 850 °C, corresponding to the end of the crystallization peak in DTA thermograms [23,27].

However, as regards BTE applications, material composition and chemical properties are not the only factors affecting the biological performances of the scaffold and, in addition, structural/microstructural parameters should be carefully considered. An ideal scaffold intended for BTE, indeed, should exhibit similar features to those of natural bone - trabecular or cortical - according to the specific implantation site. Among these, while mechanical resistance is essential to ensure a proper mechanical support over the whole bone healing process [7], intrinsic permeability is maybe one of the key factors in defining nutrient/oxygen supply and cell migration conditions through the 3D volume of the scaffold [7]. In this way, scaffold colonization by osteoprogenitor cells is favoured and new bone matrix could be synthesized inside the synthetic graft: therefore, both the material (osteo)integration and the healing process will be accelerated while ensuring a proper mass transport, which is usually one of the most critical aspects dealing with 3D tissue engineering approaches.

There is convincing experimental evidence that the scaffold porosity alone is not enough to realistically predict the efficiency of nutrient and fluid flow transportation within the 3D volume of the graft. Total porosity, in fact, includes not only open and interconnected pores, which are actually involved in mass transport mechanisms, but also closed and dead-end pores, i.e. interstitial voids between adjacent glass particles.

In the present study,  $\mu$ -CT imaging allowed us to carry out an accurate study on pore size, shape and interconnectivity, quantifying exactly the number of pores contributing to fluid flow in the volume of bioactive 47.5B glass-based scaffolds sintered at different temperatures. Pore shape factor (sphericity) and pore diameter of connected pores were also evaluated as a function of the sintering temperature.

Among all the available techniques used for bone scaffold manufacturing, maybe the replication of proper polymeric templates, like PU foams, is the one that allows obtaining the most “trabecular bone-like” morphology through a conceptually easy and affordable procedure. However, the architecture of foam-derived sintered scaffolds is not a perfect “carbon-copy” replica of the polymeric template. In this regard, Figure 9 instructively displays the relation existing between microstructure/mass transport properties of scaffolds and thermal behavior of 47.5B glass in the sintering range of 600 to 850 °C (DTA results are taken from [27]). If the sintering temperature is increased above the crystallization onset ( $T_x$ ), significant modifications occur in scaffold morphology and architecture as compared to the PU sponge, with a reduction of the pore diameter from 0.41-0.92 mm for scaffolds sintered at 600 °C to 0.17-0.28 mm for scaffolds sintered at 850 °C. The presence of larger macropores in mild sintering conditions could be easily explained by considering that the shrinkage of the material assessed by hot-stage microscopy measurements was reported to be lower than 5% for  $T < 650$  °C [26]. As a result, it was reasonable to observe a pore dimension in the final sintered scaffold (410-920  $\mu$ m) comparable to that of the original PU template, ranging between 350 and 900  $\mu$ m. Despite the higher densification of the structure, the macropore dimension of scaffolds sintered at 800 and 850 °C could still be included within the minimal range recommended for allowing cell migration and nutrients supply [7].

Interestingly,  $d_p$  data dispersion decreased with the increase in sintering temperature: this aspect could be explained by considering that the material treated at lower temperatures exhibits sub-optimal sintering between adjacent particles, which may result in an accidental breakage of trabeculae, thus determining the union between two or more pores and yielding an overall higher dispersion of pore sizes.



Pore sphericity was also found to decrease by increasing the sintering temperature, as a result of the deviation from the original template morphology characterized by tetrakaidecahedral pores.

Microstructural data obtained from  $\mu$ -CT analysis were integrated with the experimental permeability values, which were determined by an acoustic method [21] that was applied for the first time to bioactive glass-based scaffolds in the present work. Unlike the methods reported in literature up to now for assessing the permeability of biomedical scaffolds, this technique relies on the measurement of the sinusoidal pressure component, uses air instead of water as fluid media and needs a single transducer (a low-frequency pressure field microphone) to measure the pressure drop upstream and downstream of the scaffold.

Interestingly,  $k$  variation as a function of the sintering temperature followed the same trend of  $d_p$  (Figure 9) and  $\phi_p$  (Table 2), which can be therefore suggested to play a predominant role in defining the intrinsic permeability of the scaffolds. Intrinsic permeability values displayed in Table 3 were found to be definitely in the range of those of trabecular bone reported by several authors, as summarized in Table 5.

Table 5. Intrinsic permeability values of human trabecular bone.

Material	Origin/anatomical site	Permeability ( $\text{m}^2$ )	Ref
Human trabecular bone	Fresh frozen calcanei of cadavers	$0.4\text{-}11.0 \cdot 10^{-9}$	[52]
Human trabecular bone	Vertebral body	$1.5\text{-}12.1 \cdot 10^{-9}$	[53]
Human trabecular bone	Proximal femur	$0.01\text{-}4.7 \cdot 10^{-9}$	[53]

Moreover, comparable results were obtained by Ochoa et al. [54] and Li et al. [55] for Bioglass<sup>®</sup>-based scaffolds with 90-95 vol.% porosity produced by foam replica technique ( $1.96 \cdot 10^{-9} \text{ m}^2$ ) and 70 vol.% porous calcium phosphates ( $2.13 \cdot 10^{-10} \text{ m}^2$ ), respectively. In summary, these comparisons confirm the potential suitability of 47.5B-derived foam-like scaffolds for BTE applications.

The only scaffolds which did not satisfy the permeability requirements, compared to that of human spongy bone, were those sintered at 850°C, the permeability of which was 2 to 3 orders of magnitude lower. It is worth highlighting that, however, both total porosity and mean pore size of these scaffolds still were in the typical ranges reported for trabecular bone [7, 43] but, as discussed above, these two parameters alone are not enough to reliably estimate whether a scaffold is architecturally suitable or not for tissue engineering applications. In this case, in fact, the combination of several factors, including low effective porosity (40 vol.%), high pore tortuosity (1.68) and pore size close to the lower recommended limits (~100-150  $\mu\text{m}$ ), could likely determine a negative picture of the scaffold performances both *in vitro* and *in vivo*. This is a further proof of the key importance of permeability-related parameters for the final biological response resulting from the graft implantation.

Referring to Figure 9, another interesting aspect to be considered is the drop of permeability values observed in the scaffolds treated at 700°C (i.e., the onset of crystallization), where the early-stage nucleation of combeite led to a reorganization of the scaffold structure at the micro-scale, which was likely related to the higher percentage of closed porosity compared to that observed for  $T_s \geq 750^\circ\text{C}$ . However, despite samples sintered between 600 and 700°C exhibited comparable values of closed porosity and the scaffolds sintered at 700 °C was characterized by higher effective porosity, it seemed that mass transport properties remarkably decreased. In this regard, some consideration on the origin of closed pores could be crucial to clarify these only apparently conflicting results.

The formation of closed pores within open-cell structures produced by powder sintering could be due either to technological issues (i.e. less efficient sintering conducted above crystallization onset) or the persistence of interstitial porosity after sintering. Considering the scaffolds treated at 600 and 650 °C, it was reasonable to relate the presence of closed pores to interstitial spaces between particles, as clearly shown in Figure 5b. Topographical analysis performed on the scaffolds sintered at 700 °C, instead, did not reveal the presence of residual interstitial porosity (Figure 5d) and, in this case, closed porosity likely

formed from the closure of interpore window during the sintering process. At 700 °C, in fact, the shrinkage of the material upon heating was reported to be about 30 vol.% [26], determining an early collapse of the porous architecture.

The open-to-close pore ratio  $R$  was found to remain roughly constant (below 2.7) up to  $T_{s3} = 700$  °C, while it is generally higher for scaffolds sintered at higher temperature. This reveals that, at higher sintering temperature, open porosity – deriving from the template macropores - becomes strongly predominant over the closed one as the latter tend to significantly reduce, consistently with the densification behavior of the 3D structure upon thermal treatment.

According to what said up to now, scaffold behavior in biological environment is the result of a complex combination of several parameters ( $\varepsilon$ ,  $\varphi_p$ ,  $d_p$ ) and, thus, a complete and unambiguous understanding of the overall mathematical laws determining mass transport patterns is essential to predict cell response and scaffold performances *in vivo*.

The constitutive equation here proposed (section 2.2.1) was based on well-defined physical parameters, with no empirical relations. As a consequence, by using accurate input experimental data, it was possible to properly derive the scaffold physical/microstructural properties. For its correct implementation, the following assumptions and boundary conditions were defined:

- (i) The average pore diameter  $d_p$  was assumed as the characteristic length scale of the internal structure of the porous medium (also called the effective scale of microstructure [33]). As it is known, many formulations for “pore size” are available and debated in literature, on the basis of different features and morphologies of permeable media [56-59], and slightly different results can be achieved, depending on the applied model.
- (ii) Pore morphology does not vary as a function of the dynamic stresses induced by alternating fluid flow [60], as glass and glass-ceramics can be assumed as highly stiff solid materials.

- (iii) No-slip condition at airflow/pore walls interface. As a matter of fact, unlike the liquid fluid flows having no-slip boundary conditions at the solid wall, gases may slip along the solid walls because of the small scale of the pore cross-section [61]. On the other hand, when the mean free path  $\lambda$  of gas is considerably smaller compared to the pore diameter, no-slip conditions can be assumed: namely, the mean free path of air, at the atmospheric pressure, is  $\lambda \sim 0.07 \mu\text{m}$ , which is greatly smaller than scaffold pore diameters here measured [62].

Under these assumptions, the parameters provided as output of the mathematical model constituted the complete microstructural characterization of the scaffolds analyzed.

As reported in Table 4, the values of interstitial Reynolds number  $R_i$ , calculated for the proper flow linear velocity  $U$  in each scaffold, were always  $<1$ ; as a consequence, it was possible to determine the intrinsic permeability in Darcy's linear region, considering the inertial losses as negligible in comparison to the viscous ones, with a deviation from linearity lower than 1%.

At very low Reynolds number  $R_i < 1$ , the roughness and irregular shape of pore walls do not affect the flow resistance and, for laminar flow, the friction factor  $f_c$  is independent of the surface roughness and it varies linearly with the inverse of Reynolds number [43,62].

The pore morphology-dependent parameter  $\beta$  relates the pressure drop to the effects of pore cross-sectional area variation on the fluid flow [36,37]; specifically, the pressure drop decreases with increasing  $\beta$ , according to the experimental observations [63].

Experimental permeability ranges (Table 3) are in good agreement with the target ones for cancellous bone (Table 4), as a further proof of the solidity of the method and the high accuracy of permeability measurements here performed.

## 5. Conclusions

In the present study, the experimental intrinsic permeability results were combined with the detailed  $\mu$ -CT-based pores analysis in a mathematical model, in order to quantify the overall microstructural changes occurring in foam-replicated bioactive glass-derived scaffolds upon different thermal treatments.

Among all the microstructural variables investigated, pore size, shape and tortuosity were found to be the most influent in affecting scaffold permeability properties. Besides, although high-temperature sintering treatments are usually associated to a dramatic reduction of porosity resulting from the densification process of the material, scaffolds with proper mass transport properties for BTE and well-densified struts could be successfully obtained if sintering was performed below 850 °C, corresponding to the end of the crystallization process. In correspondence of this temperature, indeed, the densification deriving from the thermal treatment resulted in a combination of several microstructural features likely able to determine less favourable conditions for mass transport and cell migration phenomena to occur. The clear dependence observed between 47.5B glass characteristic temperatures and scaffold permeability variation motivates future studies on other bioactive glass compositions, in order to assess if the achievements reported in this work can have a general validity and be applicable to the entire class of bioactive glass foams.

**Conflicts of interest:** Authors declare no conflicts of interest.

## **List of Figures**

Figure 1. Schematic representation of the compression protocol followed for scaffold manufacturing.

Figure 2. The pore sphericity and the pore cross-section change, due to a throat, in the flow direction.

Figure 3. The principle of intrinsic permeability measurement by using an alternating airflow.

Figure 4. SEM images of 47.5B-based scaffolds produced by replication of commercial PU sponges. Changes in morphology due to the variation in the sintering temperature can be clearly appreciated.

Figure 5. SEM images of 47.5B scaffold surfaces at different magnification sintered at 600°C (a-b), 700°C (c-d) and 850°C (e-f). Material devitrification resulted in the formation of flower-like crystals associated to the nucleation of combeite.

Figure 6. Example of  $\mu$ -CT images of foam-replicated cylindrical scaffolds: Top, right, front views and 3D reconstruction of a 47.5B-glass scaffold sintered at 600 °C, merge threshold 95%.

Figure 7. Actual distribution of pore diameters within 47.5B scaffolds sintered at different temperatures. Each histogram represents the pore size distribution within a representative sample for each sintering group.

Figure 8. Graphical solutions of Equation 17, assessed by using experimental data of permeability  $k$  and pore diameter  $d_p$ .

Figure 9. Thermal behaviour and microstructural properties of foam replicated scaffolds: (a) DTA thermogram showing the thermal behaviour of 47.5B bioactive glass in the range 600-850 °C; (b) experimental intrinsic permeability data of the samples represented within the 1<sup>st</sup> and the 3<sup>rd</sup> quartile; (c) distributions of the equivalent hydraulic diameter of pores in the samples represented within the 1<sup>st</sup> and

the 3<sup>rd</sup> quartile; (d) distributions of the effective porosity of the samples represented within the 1<sup>st</sup> and the 3<sup>rd</sup> quartile.

## **List of Tables**



Table 1. Geometrical dimensions, physical and structural properties of 47.5B scaffolds sintered at different temperatures, expressed as mean value  $\pm$  standard deviation.

Table 2. Pore diameter: experimental data and statistical results.

Table 3. Intrinsic permeability experimental results and statistical analysis

Table 4. Microstructural and transport properties of scaffolds produced at different sintering temperatures.

Table 5. Intrinsic permeability values of human trabecular bone.

## References

- [1] A. Clegg, J. Young, S. Iliffe, M.O. Rikkert, K. Rockwood, Frailty in elderly people, *Lancet* 381 (2013) 752–762.
- [2] V. Campana, G. Milano, E. Pagano, M. Barba, C. Cicone, G. Salonna, W. Lattanzi, G. Logroscino, Bone substitutes in orthopaedic surgery: from basic science to clinical practice, *J. Mater. Sci. Mater. Med.* 25 (2014) 2445-2461.
- [3] L.L. Hench, D. Greenspan, Interactions between bioactive glass and collagen: a review and new perspectives. *J. Aust. Ceram. Soc.* 49(2013) 1-40.
- [4] D. Greenspan, Bioglass at 50 – A look at Larry Hench’s legacy and bioactive materials, *Biomed. Glasses* 5 (2019) 178–184.
- [5] L.L. Hench, Genetic design of bioactive glasses, *J. Eur. Ceram. Soc.* 29 (2009) 1257–1265.
- [6] A. Hoppe, N. Guldal, A.R. Boccaccini, Biological response to ionic dissolution products from bioactive glass and glass-ceramics in the context of bone tissue engineering. *Biomaterials* 32 (2011) 2757-2774.
- [7] L.C. Gerhardt, A.R. Boccaccini, Bioactive glass and glass-ceramic scaffolds for bone tissue engineering, *Materials* 3 (2010) 3867–3910.
- [8] F. Bairo, E. Fiume, J. Barberi, S. Kargozar, J. Marchi, J. Massera, E. Verné, Processing methods for making porous bioactive glass-based scaffolds – A state-of-the-art review, *Int. J. Appl. Ceram. Technol.* 16 (2019) 1762-1796.
- [9] Q. Fu, E. Saiz, M.N. Rahaman, A.P. Tomsia, Bioactive glass scaffolds for bone tissue engineering: state of the art and future perspectives. *Mater. Sci. Eng. C* 31 (2011) 1245–1256.

- [10] G. Kaur, V. Kumar, F. Baino, J.C. Mauro, G. Pickrell, I. Evans, O. Bretcanu, Mechanical properties of bioactive glasses, ceramics, glass-ceramics and composites: State-of-the-art review and future challenges, *Mater. Sci. Eng. C* 104 (2019) 109895.
- [11] K.A. Hing, Bioceramic bone graft substitutes: influence of porosity and chemistry *Int. J. Appl. Ceram. Technol.* 2 (2005) 184–199.
- [12] T. Hildebrand, A. Laib, R. Muller, J. Dequeker, P. Ruegsegger, Direct three-dimensional morphometric analysis of human cancellous bone: microstructural data from spine, femur, iliac crest, and calcaneus, *J. Bone Min.Res.* 14 (1999) 1167–1174.
- [13] T.M. Link, V. Vieth, R. Langenberg, N. Meier, A. Lotter, D. Newitt, S. Majumdar, Structure analysis of high-resolution magnetic resonance imaging of the proximal femur: in vitro correlation with biomechanical strength and BMD, *Calcif. Tissue Int.* 72 (2003) 156–165.
- [14] S. Hollister, E. Liao, E. Moffit, C. Jeong, J. Kemppainen, Defining design targets for tissue engineering scaffolds, in: U. Meyer (Ed.), *Fundamentals of Tissue Engineering and Regenerative Medicine*, Springer, Berlin, 2009, pp. 521–538.
- [15] V. Karageorgiou, D. Kaplan, Porosity of 3D biomaterial scaffolds and osteogenesis, *Biomaterials* 26 (2005) 5474–5491.
- [16] S. Roosa, J. Kemppainen, E. Moffitt, P. Krebsbach, S. Hollister, The pore size of polycaprolactone scaffolds has limited influence on bone regeneration in an in vivo model, *J. Biomed. Mater. Res.* 92A (2009) 359–368
- [17] M. Böhner, Y. Loosli, G. Baroud, D. Lacroix, Commentary: deciphering the link between architecture and biological response of a bone graft substitute, *Acta Biomater.* 7 (2011) 478–484.

- [18] G. Falvo D'Urso Labate, G. Catapano, C. Vitale-Brovarone, F. Baino, Quantifying the micro-architectural similarity of bioceramic scaffolds to bone, *Ceram. Int.* 43 (2017) 9443-9450.
- [19] F. Pennella, G. Cerino, D. Massai, D. Gallo, G. Falvo D'Urso Labate, A. Schiavi, M.A. Deriu, A. Audenino, U. Morbiducci, A survey of methods for the evaluation of tissue engineering scaffold permeability, *Ann. Biomed. Eng.* 41 (2013) 2027-2041.
- [20] ASTM F2952 – 14. Standard Guide for Determining the Mean Darcy Permeability Coefficient for a Porous Tissue Scaffold
- [21] A. Schiavi, C. Guglielmone, F. pennella, U. Morbiducci, Acoustic method for permeability measurement of tissue-engineering scaffold, *Meas. Sci. Technol.* 23 (2012) 105702
- [22] E. Fiume, G. Serino, C. Bignardi, E. Verné, F. Baino. Bread-derived bioactive porous scaffolds: an innovative and sustainable approach to bone tissue engineering, *Molecules* 24 (2019), 2954.
- [23] E. Fiume, D. Tulyaganov, G. Ubertalli, E. Verné, F. Baino, Dolomite-foamed bioactive silicate scaffolds for bone tissue repair, *Materials* 13 (2020) 628.
- [24] E. Fiume, C. Migneco, E. Verné, F. Baino, Comparison between bioactive sol-gel and melt-derived glasses/glass-ceramics based on the multi-component  $\text{SiO}_2\text{--P}_2\text{O}_5\text{--CaO--MgO--Na}_2\text{O--K}_2\text{O}$  system. *Materials* 13 (2020) 540.
- [25] Q.Z. Chen, I.D. Thompson, A.R. Boccaccini, 45S5 Bioglass®-derived glass–ceramic scaffolds for bone tissue engineering, *Biomaterials* 27 (2006) 2414-2425.
- [26] J. Barberi, F. Baino, E. Fiume, G. Orlygsson, A. Nommeots-Nomm, J. Massera, E. Verné. F, Robocasting of  $\text{SiO}_2$ - based bioactive glass scaffolds with porosity gradient for bone regeneration and potential load-bearing applications, *Materials* 12 (2019) 2691.

- [27] E. Fiume, E. Verné, F. Bairo. Crystallization behavior of  $\text{SiO}_2\text{--P}_2\text{O}_5\text{--CaO--MgO--Na}_2\text{O--K}_2\text{O}$  bioactive glass powder, *Biomed. Glasses* 5 (2019) 46-52.
- [28] O. Reynolds, An experimental investigation of the circumstances which determine whether the motion of water shall be direct or sinuous, and of the law of resistance in parallel channels. *Philos. Trans. R. Soc. Lond.* 174 (1883) 935-982.
- [29] P. Forchheimer, Wasserbewegung durch boden, *Zeit. Ver. Deut. Ing.* 45 (1901) 1782-1788.
- [30] S. Ergun, Fluid flow through packed columns, *Chem. Eng. Prog.* 48 (1952) 89-94.
- [31] R.K. Niven, Physical insight into the Ergun and Wen & Yu equations for fluid flow in packed and fluidised beds, *Chem. Eng. Sci.* 57(2002) 527-534.
- [32] L. Xianke, Y. Zhao, and D.J.C. Dennis, Flow measurements in microporous media using micro-particle image velocimetry, *Phys. Rev. Fluids* 3 (2018) 104202.
- [33] M.V. Chor, W. Li, A permeability measurement system for tissue engineering scaffolds, *Meas. Sci. Technol.* 18 (2007) 208-216.
- [34] H. Wadell, Sphericity and roundness of rock particles, *J. Geol.* 41 (1933) 310-331.
- [35] J. Zheng, R.D. Hryciw, Roundness and sphericity of soil particles in assemblies by computational geometry, *J. Comput. Civil Eng.* 30 (2016) 04016021.
- [36] J. Wu, B. Yu, M. Yun, A resistance model for flow through porous media, *Transp. Porous Med.* 71 (2008) 331-334.
- [37] Wu, J., Hu, D., Li, W., & Cai, X. (2016). A review on non-Darcy flow—Forchheimer equation, hydraulic radius model, fractal model and experiment. *Fractals*, 24(02).
- [38] B. Yu, J. Li, A geometry model for tortuosity of flow path in porous media, *Chin. Phys. Lett.* 21 (2004) 1569-1571.

- [39] A. Koponen, M. Kataja, J.V. Timonen, Tortuous flow in porous media, *Phys. Rev. E* 54 (1996) 406.
- [40] A. Koponen, M. Kataja, J.V. Timonen, Permeability and effective porosity of porous media, *Phys. Rev. E* 56 (1997) 3319.
- [41] K. Rasmussen, Calculation methods for the physical properties of air used in the calibration of microphones, Report No. PL-11b, Technical University of Denmark, Lyngby, Denmark, 1997.
- [42] F. Baino, J. Barberi, E. Fiume, G. Orlygsson, J. Massera, E. Verné, Robocasting of Bioactive  $\text{SiO}_2$ - $\text{P}_2\text{O}_5$ - $\text{CaO}$ - $\text{MgO}$ - $\text{Na}_2\text{O}$ - $\text{K}_2\text{O}$  Glass Scaffolds, *J. Health. Eng.* 8 (2019) 1-12.
- [43] S. Yang, K.F. Leong, Z. Du, C.K. Chua, The design of scaffolds for use in tissue engineering. Part I. Traditional factors, *Tissue Eng.* 7 (2001) 679–689.
- [44] C. Navalón, P. Ros-Tárraga, A. Murciano, P. Velasquez, P. Mazón, P. N. De Aza. Easy manufacturing of 3D ceramic scaffolds by the foam replica technique combined with sol-gel or ceramic slurry, *Ceram. Inter.* 45 (2019) 18338-18346.
- [45] F.S. Kaplan, W.C. Hayes, T.M. Keaveny, A. Boskey, T.A. Einhorn, J.P. Iannotti, Form and function of bone. In: S.R. Simon, Editor, *Orthopaedic basic science*, Rosemont: American Academy of Orthopaedic Surgeons (1994) 128–84.
- [46] J. Henkel et al. Bone Regeneration Based on Tissue Engineering Conceptions – A 21st Century Perspective. *Bone Res.* 3 (2013) 216-248.
- [47] Q. Fu, M.N. Rahaman, B.S. Bal, R.F. Brown, D. E. Day. Mechanical and in vitro performance of 13–93 bioactive glass scaffolds prepared by a polymer foam replication technique, *Acta Biomater.* 4 (2008) 1854-1864.

- [48] J.A. Hipp, A. Jansujwicz, C.A. Simmons, B.D. Snyder, Trabecular bone morphology from micro-magnetic resonance imaging, *J. Bone. Miner. Res.* 11(1996) 286-292.
- [49] O. Bretcanu, X. Chatzistavrou, K. Paraskevopolous, R. Conradt, I. Thompson, A.R. Boccaccini. Sintering and crystallisation of 45S5 Bioglass<sup>®</sup> powder. *J. Eur. Ceram. Soc.* 29 (2009), 3299–3306.
- [50] E. Verné, O. Bretcanu, C. Balagna, C.L. Bianchi, M. Cannas, S. Gatti, C. Vitale-Brovarone, Early stage reactivity and in vitro behavior of silica-based bioactive glasses and glass-ceramics, *J. Mater. Sci. Mater. Med.* 20 (2009) 75-87.
- [51] M.J. Grimm, J.L. Williams, Measurements of permeability in human calcaneal trabecular bone, *J. Biomech.* 30 (1997) 743-745.
- [52] E.A. Nauman, K.E. Fong, T.M. Keaveny. Dependence of intertrabecular permeability on flow direction and anatomic site, *Ann. Biomed. Eng.* 27 (1999) 517-524.
- [53] I. Ochoa, J.A. Sanz-herrera, J.M. Garcia-Aznar, M. Doblaré, D.M. Yunos, A.R. Boccaccini. Permeability evaluation of 45S5 Bioglass-based scaffolds for bone tissue engineering, *J. Biomech.* 42 (2009) 257-260.
- [54] S. Li, J.R. De Wijn, J. Li, P. Layrolle, K. De Groot. Macroporous biphasic calcium phosphate scaffolds with high permeability/porosity ratio, *Tissue Eng.* 9 (2003) 535-546.
- [55] M.A. Biot, Mechanics of deformation and acoustic propagation in porous media, *J. Appl. Phys.* 33(1962)1482-1498.
- [56] D. Edouard, M. Lacroix, C.P. Huu, F. Luck, Pressure drop modeling on SOLID foam: State-of-the art correlation, *Chem. Eng. J.* 144 (2008) 299-311.
- [57] A. Inayat, M. Klumpp, M. Lämmermann, H. Freund, W. Schwieger, Development of a new pressure drop correlation for open-cell foams based completely on theoretical grounds: Taking into account strut shape and geometric tortuosity, *Chem. Eng. J.* 287 (2016) 704-719.

- [58] K. Prashant, F. Topin, Influence of Morphology on Flow Law Characteristics in Open-Cell Foams: An Overview of Usual Approaches and Correlations, *J. Fluids Eng.* 139 (2017) 071301.
- [59] P. Kumar, F. Topin, State-of-the-art of pressure drop in open-cell porous foams: review of experiments and correlations, *J. Fluids Eng.* 139 (2017) 111401-111413.
- [60] L. Shijie, J. H. Masliyah, Principles of single-phase flow through porous media, *Adv. Chem.* 251(1996) 227-286
- [61] P. Sridhar, S. Aliabadi, Computational study of no-slip and rarefied slip flows in infinite structured porous media, *Comput. Fluids.* 136 (2016) 485-496.
- [62] Brkić, Dejan, and Pavel Praks. "Unified friction formulation from laminar to fully rough turbulent flow." *Applied Sciences* 8.11 (2018): 2036.
- [63] J. P. Du Plessis, Analytical quantification of coefficients in the Ergun equation for fluid friction in a packed bed, *Trans. Porous Media* 16 (1994) 189– 207